

Bucknell University

Bucknell Digital Commons

Faculty Journal Articles

Faculty Scholarship

2-2023

A Narrow-channeled Backward-facing Step Flow With or Without a Pin-fin Insert: Flow in the Separated Region

James K. Arthur

Bucknell University, jka012@bucknell.edu

Follow this and additional works at: https://digitalcommons.bucknell.edu/fac_journ

Recommended Citation

Arthur, James K.. "A Narrow-channeled Backward-facing Step Flow With or Without a Pin-fin Insert: Flow in the Separated Region." (2023) .

This Article is brought to you for free and open access by the Faculty Scholarship at Bucknell Digital Commons. It has been accepted for inclusion in Faculty Journal Articles by an authorized administrator of Bucknell Digital Commons. For more information, please contact dcadmin@bucknell.edu.

A narrow-channeled backward-facing step flow with or without a pin-fin insert: flow in the separated region

James K Arthur^{†1}

[†]Department of Mechanical Engineering

Bucknell University

1 Dent Dr, Lewisburg PA, 17837, USA

Abstract

This paper reports an experimental investigation of the separated flow region of a backward-facing step (BFS) turbulent flow. The goal was to characterize the three-dimensional flow field in a narrow BFS channel with or without a pin-fin insert. Consequently, a closed BFS channel of an expansion ratio 1.25 and aspect ratio 8.0 was tested. The pin-fin inserts employed were of 85% porosity, and of rod height similar to the step height h . The Reynolds number of the in-coming flow based on the center-line mean streamwise velocity and h was maintained at 6000. The presence of the insert and its location behind the step was also varied from $0.69h$ to $15.58h$. Using a planar particle image velocimetry, detailed velocity measurements were made across several spanwise planes within the entry and separated regions of the test section. The results show asymmetric qualities of reattachment length, vorticity and turbulent statistics about the spanwise plane. It is also evident that the use of inserts directly behind the step transforms the flow into one without any separated section. However, by varying the insert between $2.9h$ and $15.6h$, the extent of the recirculation zone can be modulated between 56% to 108% of the length that exists without inserts. Additionally, the inserts may be used to enhance turbulent production while creating regions of energy sink. Apart from the physics unveiled in this study, the data presented provide valuable benchmark for validation, as well as suggestions to build more robust turbulent models to simulate narrow-channeled BFS flows.

Keywords – Backward-facing step, separated region, particle image velocimetry, pin-fin insert, turbulent flow, porous model

¹ Author to whom correspondence may be directed. Email: james.arthur@bucknell.edu

1. Introduction

In thermal-fluid systems such as combustor flame-holders, blades of turbines, and engine inlets, sudden expansion or backward facing step (BFS) flows are widely encountered. For such flows, the general features are as follows [1]. Flow from an upstream region approaches the BFS with a defined boundary layer. Upon leaving the step, the flow encounters a separated region. Here, the presence of an adverse pressure gradient results in a wake flow marked by a thin but growing separated shear layer. Due to the strong pressure gradient and the concomitant upstream deflection of fluid from the shear layer, a region of flow reversal (or recirculation) is formed between the shear layer and adjacent walls. This recirculation region is often identified by one or more separation vortices or recirculation bubbles. However, as more fluid is entrained, a more favorable pressure gradient is gained. This leads to the down-curving of the shear layer toward the bottom wall and an ultimate reattachment on the wall. Further downstream, the unobstructed reattached flow undergoes a recovery region where it redevelops into a new boundary layer after several step heights.

The nature of the separated and recovery regions is complex. Thus, they have been the subject of several experimental, numerical and analytical research studies. An early focus of these studies was to consider *plain BFS configurations*, and to determine the effects of geometric and flow conditions on parameters such as the reattachment length (i.e. the streamwise length between the step and the location of re-attachment), low and high order turbulence statistics and their derivatives, skin friction coefficient, and wall friction coefficients. Among the conditions that have been considered are the aspect ratio (i.e. AR, which is the ratio of channel width to step height), expansion ratio (i.e. ER, which is the ratio of the test channel depth before the step to the that after the step), pressure gradient, flow regime of the upstream boundary layer (usually defined by the Reynolds number Re based on the maximum or centerline velocity of the entry flow, and the step height or momentum thickness), perturbation strength (i.e. the ratio of the entry boundary layer thickness to step height), and the freestream turbulence. While fundamental studies on plain BFS flows are still on-going, a later effort has been concentrated on more *intricate BFS flow configurations* incorporating modifications such as suction or blowing across wall, flapping foils, and inserts. These research works have been pursued with the view to exploring various mechanisms by which BFS flows may be controlled or modified for specific purposes such as heat transfer enhancement.

One of the most important findings of previous works on plain BFS flows is that for flow arrangements of $AR > 10$, there is negligible secondary flow side wall effects on the channel's mid-span flow characteristics [2], [3]. The implications of this conclusion for simplified flow analysis and measurement have influenced the overwhelming tilt of subsequent investigations on large aspect ratio channels. Thus, much of the physics of flow of BFS is known from such (two-dimensional) works. In one such seminal study for instance, Armaly et al. [4] used a plain BFS channel of $AR = 36$ to evaluate important variations in the flow domain as the regime changes from laminar to turbulence. They observed that while the separation length increases non-linearly with Re in the laminar regime, it declines sharply during regime transition, and remains constant at full turbulence. Driver and Seegmiller [5] also tested a BFS model of $AR = 12$ with the top wall capable of being modified in angle of inclination from the trailing edge of the step from 0 to 10° . Their tests revealed that the reattachment length and spread rate of the shear layer increase with wall divergence (or adverse pressure gradient) while yielding insignificant effects on the Reynolds stresses and triple velocity products. Isomoto and Honami [6] subsequently tested a BFS channel of $AR = 18$. They used a cavity or rod upstream of the step to determine the effect of turbulence intensity changes of the approach flow on the downstream flow. Isomoto and Honami [6] demonstrated that an increase in the maximum turbulence intensity near the wall at the separation point tends to reduce the reattachment length. In one of the first most detailed whole-field measurements of BFS flows, a channel of $AR = 20$ was used [7]. Particle-tracking velocimetry was used in the measurement. Nadge and Govardhan [8] also used a particle image velocimetry (PIV) technique to study the effects of ER in a BFS flow. In that work also, test channels of large AR ($16 \leq AR \leq 60$) were used to show that the reattachment length increases at a nearly linear rate for $ER < 1.8$. In a more recent set of studies, large AR BFS channels have been used to study the effects of surface roughness [9] and coherent vortex structure of the flow in the recirculation region [10]. In summary, BFS flows have been customarily modeled using channels with AR greater than 10.

Apart from a few exceptions (e.g. ref. [11]), even in the case of BFS flow control / modification studies, the preponderance of works is still skewed towards measurements in large AR channels. Lai et al. [12] for instance tested the utility of a 10 mm NACA 0012 airfoil as an active means of flow control in a BFS of $AR = 12.33$. By flapping the foil at 20 Hz, they showed that a 70% reduction of the reattachment length may be achieved if the flap is located in close proximity to the step and wall. In another study of active flow control method, Sano et al. [13] used a suction

mechanism through a slit at the bottom corner of the step in a BFS of $AR = 12.67$. They noted that the heat transfer coefficient in the recirculation region was enhanced through suction. This enhancement was observed to be associated with large scale turbulent motion, strong mixing, Reynolds shear stress and turbulent diffusions. To modify the flow without any external energy requirement, passive methods have been also explored almost entirely on the basis of a two-dimensional analysis. In one representative case, Cheng and Tsay [14] simulated a laminar flow problem with a baffle in a two-dimensional space. They concluded that while solid baffles lead to an increment in heat transfer, they may cause a re-separation of the flow and a poor local heat transfer coefficient in the heating section. This problem is however improved when the baffle is slotted [14]. Porous inserts have also been reported to change location, shape and size of recirculating bubbles of BFS flows [15]. Nevertheless, even in such studies, assessments have been conducted using two-dimensional analysis. Indeed, it is fair to say that the only relevant studies on porous inserts in BFS are laminar [16]-[19] or two-dimensional turbulent flow studies [15], [20].

On the other hand, a smaller number of works have focused on three-dimensional BFS flows (or BFS flows in narrow channels) [1], [21]. Even so, most of these studies entail tests conducted with point-wise measurement techniques [1], [22]-[25], or numerical simulations [21], [26], [27]. Consequently, only a handful of detailed multicomponent whole flow-field measurements of BFS flows in narrow channels are reported [28], [29]. Thus, current knowledge about three-dimensional turbulent structural effects are deficient, and empirical data for numerical validation of narrow-channeled BFSs are limited. This is a significant lack, giving that internal flows systems such as turbine blade cooling channels with ribs [30] or compact electronic cooling devices may have aspect ratios less than 10. Another deficiency in the BFS flow literature also lies in the lack of studies that explore the use of porous inserts in narrow channels.

In light of the deficits described, this work is a unique contribution to the existing literature in at least two ways. Firstly, it provides a sample detailed whole flow-field experimental study of the nature of the turbulent BFS flow field and structure in a narrow channel. More importantly, it offers a rare look at the effect of using a porous insert to modulate the turbulent flow. The goal of the study is thus to characterize and investigate the multi-component three-dimensional flow field of a turbulent flow over a BFS with or without porous inserts.

In this study, attention is focused on the effect of the pin-fin insert on the separated region. This is worthy of special devotion given that this region is often characterized by changes in momentum

and thermal transport which in turn have great impact on the average convective heat transfer values of the system [31]. Furthermore, the near-stagnation recirculation zone within this region is a source of undesirable localized cooling or heating, and substantial head losses, thereby ultimately reducing the energy efficiency of BFS flow systems [15]. Thus, it is necessary to understand the flow in the separated region in its three-dimensional form and to assess the effects of installing a porous-like insert. The analysis drawn from the mean flow data as well as single-point turbulence statistics, do serve a key foundational utility of helping to understand the flow structure. To the authors' knowledge, the test results presented here are not found anywhere else in the literature. Thus, they will find ready use in developing, validating and corroborating flow modeling tools.

The current study is accomplished through a series of tests of turbulent flow over a BFS closed channel of ER 1.25, AR 8.0 and a fixed Reynolds number Re_h (based on the step height, and the center-line mean streamwise velocity at the entrance) of ~ 6000 . The AR of the channel was used primarily due to its availability and suitability for our experimental system. However, it also serves to extend assessments of other salient effects in narrow-channeled BFS flows. Additionally, the porous insert used in this work is an array of pin-fin rods of porosity 85%. This follows in the rank of similar porous media models used in previous studies [32]-[34]. The particular model and porosity type have been selected due to the model's utility as an optimal means of improving heat transfer in other applications [35]. In the present work, the effects of the insert are measured by varying the location of the insert on the bottom wall of the expanded channel. Data is obtained through two-dimensional two-component PIV measurements.

This paper is structured as follows. A description of the experimental system and measurement procedure is given in Section 2. The experimental results are then presented and discussed in Section 3. Finally, a summary of the main conclusions of the work is outlined in Section 4.

2. Experimental System and Measurement Procedure

2.1 Test Facility

A model test channel with a backward-facing step (BFS) was used to conduct the experiments. This was built from 6 mm-thick transparent acrylic plates, and fabricated as a closed channel of internal dimensions 2500 mm (length), 70 mm (width W) and 43 mm (depth H_d). An upstream depth H_u of 34.4 mm was set at the entry section of the channel using a smooth acrylic plate, fixed on the bottom wall of the channel over a 1200 mm entry length. With the step of $h = 8.7$ mm offered at the trailing edge of the entry bottom plate, an expansion ratio $ER (= H_d / H_u)$ of ≈ 1.25 , and an aspect ratio $AR (= W/h)$ of ≈ 8.0 was achieved. As this AR of the channel is less than 10, the BFS was taken to be narrow [30]. In order to guarantee the rapid development of the turbulent boundary layer, fourteen equally spaced out square rods were glued on the first 90 mm portion of the channel to serve as trips. The entire model BFS test channel was firmly installed into an open flow transport recirculating channel supplied by *TecQuipment* Ltd. Further details of this flow transport channel are presented elsewhere [36].

It should be noted that the downstream length of the test channel was designed to allow for the installation of various geometric test conditions. As shown in Table 1, these were done to respectively simulate conditions of a BFS configuration without a porous insert, and with porous inserts. The non-insert condition was achieved using a smooth acrylic plate installation. The porous insert conditions, on the other hand, were modeled using pin-fin models. Each model was assembled by mounting transparent acrylic rods in holes drilled into a bottom wall plate. Square arrays of rods of average height $h_r = 9.06$ mm, diameter $d = 3.18$ mm, and equidistant spacing $l = 7.2$ mm between adjacent rod centers, were used. With such dimensions, the inserts were of similar height as the BFS step, and the porosity of each porous insert model could be set at 85%. In each case, twelve rows and nine columns of rods were used in order to maintain a compactly sized porous medium required for optimal heat transfer augmentation [18]. The only distinction between the models was that the center of the most upstream column of rods were respectively located at $m = 0.63h$, $2.93h$, $4.65h$, $6.95h$, $9.25h$, $10.28h$, and $15.58h$ downstream of the step. For brevity, each of these cases will be referred to as P-1, P-3, P-5, P-7, P-9, P-11, P-13, and P-15 models, correspondingly. The non-insert on the other hand, is hereafter referred to as NP model. Summary of the geometric conditions are shown in Table 1.

In Figure 1, a schematic diagram of the test channel along with the porous model is presented. The Cartesian coordinate system shown in the figure identifies the origin of the streamwise axis (i.e. $x = 0$) as fixed 1200 mm away from the flow entry and coincident at the edge of the BFS. For the wall-normal direction, its origin (i.e. $y = 0$) is at the bottom wall, while that of the spanwise direction ($z = 0$) is in the middle of the span of the channel.

2.2 Velocity Measurement System, Method of Measurement and Uncertainty Limits

Velocity data was acquired with a two-dimensional two-component particle image velocimetry (PIV) system supplied by *LaVision* Inc. This system was used in a transparent flow section with water as the working fluid, and silver-coated hollow glass spheres of mean diameter $10\mu\text{m}$ and specific gravity 1.4 as the seeding particles. The PIV hardware itself was made up of a laser, camera, programable timing unit (PTU), and a computer. A laser of 532nm wavelength and 200 mJ/pulse generated by a *Quantel Evergreen* Nd:YAG Dual Cavity system was used to illuminate the flow. An approximately 1 mm sheet of light was achieved through a set of cylindrical lenses connected to the laser. Digital images were captured and recorded as digital images using a 12-bit charged couple device camera (Imager SX 6M) with a 2752×2200 -pixel array, and $7.4\ \mu\text{m}$ pixel pitch. The camera was coupled to a 50-mm focal length *Nikon* lens, fitted with an orange filter of a band-pass wavelength of $532\ \text{nm} \pm 10\ \text{nm}$. The PTU allowed for the synchronization of the laser trigger and camera recording rates. Consequently, images were transferred to a dual processor computer with a 32-gigabyte random access memory. With the PIV software (*DaVis-10.2*) installed on the computer, the PIV system could be controlled, and the acquired data processed using a multi-pass cross-correlation algorithm. Additional analysis and plotting were done using MATLAB, OriginLab and TecPlot 360 software.

TABLE 1: Summary of geometric model parameters and PIV plane measurement locations.

Geometric test model	Distance of most upstream rods from step, m/h	Porosity of model ε	Measured spanwise plane within streamwise range $-5.5 < x/h < 5.0$	Measured spanwise plane streamwise range $0.9 < x/h < 9.6$	Measured spanwise plane streamwise range $8.3 < x/h < 18.8$
NP	-	1.00	$z/h = 0$	$-3.65 \leq z/h \leq 3.65$ at intervals of $z/h = 0.18$	$z/h = 0$
P-1	0.63	0.85	$z/h = 0$	$z/h = 0$	$z/h = 0$
P-3	2.93	0.85	$z/h = 0$	$z/h = 0$	$z/h = 0$
P-5	4.65	0.85	$z/h = 0$	$z/h = 0$	$z/h = 0$
P-7	6.95	0.85	$z/h = 0$	$z/h = 0$	$z/h = 0$
P-9	9.25	0.85	$z/h = 0$	$z/h = 0$	$z/h = 0$
P-11	10.98	0.85	$z/h = 0$	$z/h = 0$	$z/h = 0$
P-13	13.28	0.85	$z/h = 0$	$z/h = 0$	$z/h = 0$
P-15	15.58	0.85	$z/h = 0$	$z/h = 0$	$z/h = 0$

A number of precautionary measures were taken to ensure that the test system was sufficiently optimized for PIV measurements. In order to ensure that the seeding particles were neutrally buoyant in water, the particles were assessed using the settling velocity and response time parameters [37]. They are estimated to be $21.8 \mu\text{ m/s}$ and $2.2 \mu\text{ s}$, respectively. These values are extremely small compared to the mean velocities and sampling time used in the tests, thus it was projected that the seeding particles would faithfully follow the fluid flow. To minimize glare and reflections on surfaces within the flow section, dark background plates and tapes were applied on selected walls of the channel and model. Other measures were taken to allow sufficient illumination of the whole flow section, maintain particle displacements that are less than a quarter of the

interrogation area, and to reduce velocity gradient bias errors and peak-locking. They are similar to that discussed in an earlier publication [36], and will not be repeated here.

A field of view of $91.4 \text{ mm} \times 73.0 \text{ mm}$ was used in the x and y directions respectively. As such, the scale factor of the measurement is 30 pixels per mm. As this is comparable with the size of interrogation area used by Essel and Tachie [9], turbulence intensity outcomes are expected to be reasonably low in noise level. For this work, the image sampling rate was set at 4Hz per measurement. Four thousand instantaneous image pairs were acquired and used in the analysis, guaranteeing statistical convergence. In processing the data, extraneous portions of the images were masked out, leaving only the flow section. The initial interrogation area was set to a size of $64 \text{ pixels} \times 64 \text{ pixels}$, and then after several iterations and an outlier-removal validation step, each interrogation window was also subdivided into $32 \text{ pixels} \times 32 \text{ pixels}$. With a 75% overlap set between immediate interrogation areas, the distances in both x and y directions between neighboring vectors in physical units are 0.27 mm ($= 0.03h$). The resolution was assessed in terms of the smallest scales of flow, following the procedure used by Piirto et al. [29]. Accordingly, the ratio of vector spacing to the Kolmogorov length scale was estimated to be 8 which is also comparable with that utilized by Essel and Tachie [9] (i.e. 6).

In this paper, time-averaged velocities and other turbulence statistics are reported. The components of these averaged velocities, turbulence intensities, and Reynolds normal stresses in the streamwise and wall-normal directions are respectively indicated by (U, V) , (u, v) , and (u^2, v^2) . The Reynolds shear stress is also signified by $-uv$. With respect to error, it is noted that while the accuracy of velocity measurement is affected by a number of factors such as the response to fluid motion, velocity gradient, light pulse timing and sheet positioning, most of them were kept minimal by following optimization techniques referenced in previous paragraphs. Thus, uncertainties and their propagation in the velocity measurements were assessed following work of Wieneke [38]. This method applies a correlation statistical analysis of the differences in the intensity patterns of images, a primary source of error. Accordingly, it was determined that the errors of (U, V) , (u, v) , (u^2, v^2) , and $-uv$ are approximately $\pm 1.8\%$, $\pm 2.3\%$, $\pm 2.5\%$, and $\pm 3.5\%$ of their respective peak values. Errors of the turbulent kinetic energy budget estimates are no better than $\pm 7.5\%$ of their maxima. These uncertainty estimates are rated at 95% confidence level.

2.3 Preliminary Tests, Test Conditions and Entry Flow Qualification

In general, three ranges of PIV measurements were conducted to scan the entry, recirculation and preliminary redevelopment sections of the BFS flows. However, as noted in Table 1, velocity measurements were taken along several spanwise planes of the test section. This was done in order to quantify the spanwise variations of the low aspect ratio BFS channel flow. To achieve this, the laser and the camera were fixed on a translation stage. In this way, both hardware could be traversed together along the stream and across the span of the channel with a least count of ± 0.5 mm, without changing the distance between the laser and camera. In all, 43 spanwise measurements are reported for the NP model, and 24 for the porous insert models. Several other planar measurements were made in order to verify and compare results, but are omitted here to maintain conciseness.

The current tests were aimed at studying the three-dimensional turbulent flow in a narrow-channeled BFS with or without a pin-fin rod. To facilitate this goal, it was convenient to maintain entry flow conditions. Previous works have indicated that for flows with entry conditions of step Reynolds number $Re_h > 4700$, the flow is fully turbulent, and that any variations in reattachment length with Re_h , is expected to fall within error limits [4], [8]. To corroborate this for the current narrow-channeled BFS flow system, a preliminary test was carried out to determine the changes in reattachment length L_r over Re_h ranging from 3700 to 10300. For the present three-dimensional flow, the mean point of reattachment was determined as an average location, obtained by using two methods [7], [23], [24]: (1) a linear extrapolation of the zero streamwise velocity curve (hereafter called the U_o line) passing through the primary recirculation bubble, and curving toward the wall; and (2) the forward flow fraction method. The results of the evaluation are shown in Figure 2 as a profile of Re_h and the normalized reattachment length parameter L_r/h . The uncertainty in L_r is estimated to be $\pm 0.15h$. As shown, for $Re_h < 4500$, L_r/h changes by just about 2% of the mean value (i.e. 6.4) obtained for that range of Re_h . Thus, it was sufficient to fix the substantive measurements at a single value of Re_h above 4500, to study requisite effects at a fully turbulent flow regime.

To this end, the entry flow mean bulk velocity ($U_b = 0.596$ m/s) was set at constant for the test conditions under study so as to achieve full turbulence. The entry flow data extracted at the step shoulder of the plain BFS case is plotted in Figure 3. In Figure 3(a), the streamwise velocity component is plotted in outer coordinates. It is noted that U_e is the mean streamwise velocity extracted from the center-line ($H_u/2 = \delta$) within the midspan plane. This velocity was found to be 0.691 m/s. Thus, the characteristic step Reynolds number $Re_h = U_e h / \nu$ is ~ 6000 for an

approximated kinematic viscosity of water ν of $1 \times 10^{-6} \text{ m}^2/\text{s}$. The ratio U_e / U_b being 1.16, is in excellent agreement with Dean's correlation [39] (i.e. $1.28 \text{ Re}_b^{-0.0116} = 1.15$, where $\text{Re}_b = U_b H_u/\nu$). From Figure 3(a), a boundary layer displacement thickness of 7.2mm and a momentum thickness of 5.3mm was obtained, thus indicating a shape factor of 1.35. These ratios suggest that at the test Re_h , the entry flow is fully turbulent. The streamwise and wall-normal turbulence intensities are also plotted in outer coordinates in Figure 3(b). The plots show that the relative background turbulence level ($u/U_e, v/U_e$) at δ is approximately 5% and 4% respectively in the x and y directions. They do reasonably compare with previous work [9].

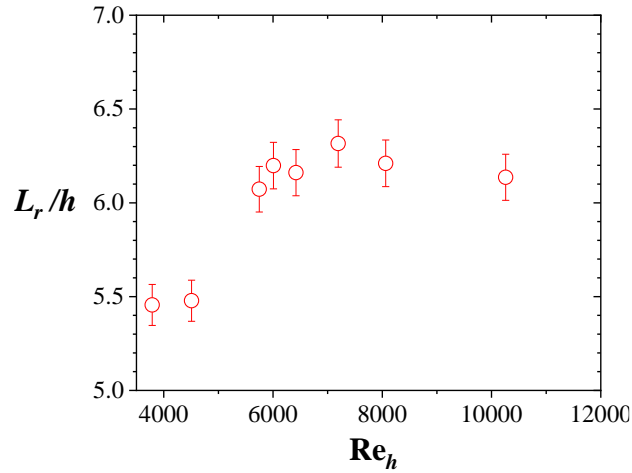


Figure 2: Changes of the normalized reattachment length L_r/h with the step Reynolds number Re_h .

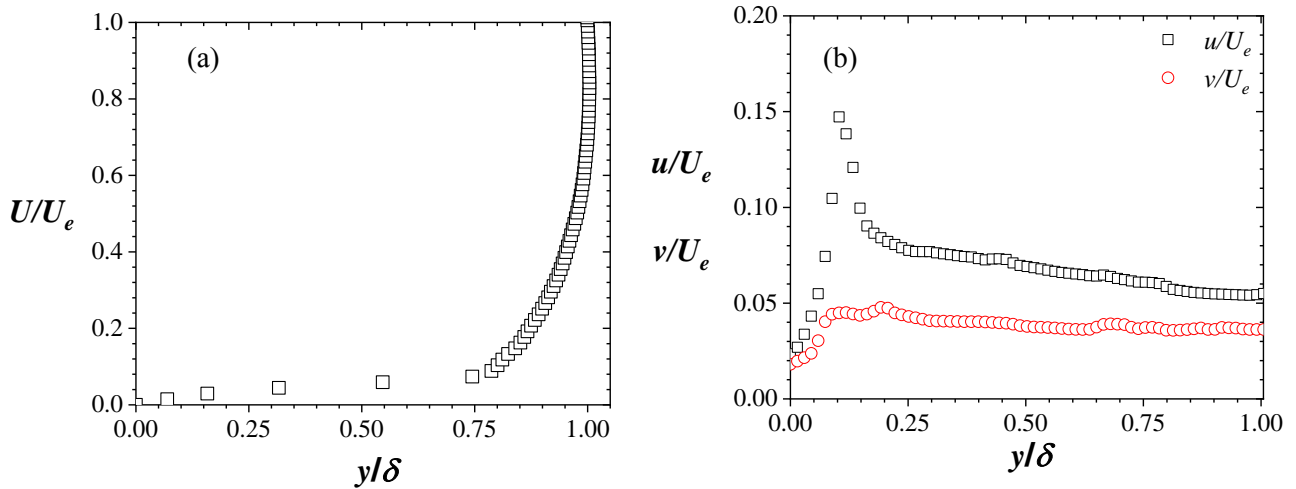


Figure 3: Streamwise component of the mean entry flow U in (a) outer coordinates (U normalized by the centerline mean streamwise velocity U_e and y is normalized by half of the upstream channel depth δ); and (b). Streamwise and wall-normal components of the root mean squared velocities (u and v respectively) in outer coordinates.

3. Results and Discussion

3.1 Three-Dimensional Effects of the Plain Narrow-Channeled BFS

In order to visualize the three-dimensional changes in the plain narrow-channeled BFS flow, the mean and turbulent flows of the recirculation region are examined. The mean flow is first considered using streamlines for the midspan flow. It is shown in Figure 4(a). The figure reveals that within this flow reversal region, the midspan flow patterns have a primary recirculation bubble, and a secondary recirculation bubble at the corner of the step. This general feature is comparable with that observed in other two-dimensional BFS flows. To assess the spanwise variations of the streamline features, the extents of the recirculation region are examined using the reattachment length (L_r) parameter. The L_r parameter is determined using methods described in Section 2.3. The zero streamwise velocity line (i.e. U_o , shown in red) is indicated in Figure 4(a) to help trace the mean reattachment location in that sample streamline plot. The results of L_r are summarized in the spanwise variation plots in Figure 4(b). The plots show that in the midspan plane, L_r/h is 6.2. This is a different result compared with the 5.8 value obtained by Essel and Tachie [9]. This is an important observation, giving that the latter was conducted in a channel of an expansion ratio similar to the current work, but of a much larger aspect ratio (i.e. $AR = 21$). Thus, the difference between that and the current work may be attributed to an acute three-dimensional channel effect.

Other three-dimensional effects are also apparent in the variation of L_r/h across the span. Compared with the midspan, the deviations initially appear small, but they reach a maximum of 11 to 14% at locations close to the side walls (i.e. $z/W < -0.36$ and $z/W > 0.36$). The changes are also asymmetric about the midspan plane. In further analysis, the streamwise and wall-normal loci of the centers of the primary and secondary recirculation bubbles are also tracked across the spanwise measurements, and plotted in Figure 4(b). The data reveals that the loci of the centers of the primary and secondary bubbles are affected by the spanwise locations. Notably, the secondary bubble in the midspan plane largely disappears at $z/W < -0.25$ and $z/W > 0.25$.

To evaluate the present results with previous studies, comparisons are made with published L_r assessments that have also explored side-wall effects. The contrasts are shown in Figure 4(c) as a ratio of L_r/L_{r_0} where L_{r_0} is the L_r at the midspan. A major observation of the plots is that the variations are asymmetric along the midspan $z/W = 0$. However, the shapes of the profiles around the sidewalls are different, apparently depending primarily on the aspect ratio. Thus, close to the sidewalls of the channel, the profile for the current measurements is similar in shape to those of Nie

and Armaly [24], which were also obtained using BFS channels of AR = 8 and expansion ratio, ER of 2. However, these are in contrast with that of Shih and Ho [23] whose study was conducted using a channel of AR and ER = 3. An additional note about the figure is that the three-dimensional effects are magnified by differences in flow regime. In particular, variations in L_r across the span appear to decrease with increasing Reynolds number in either laminar, transitional or turbulence regimes.

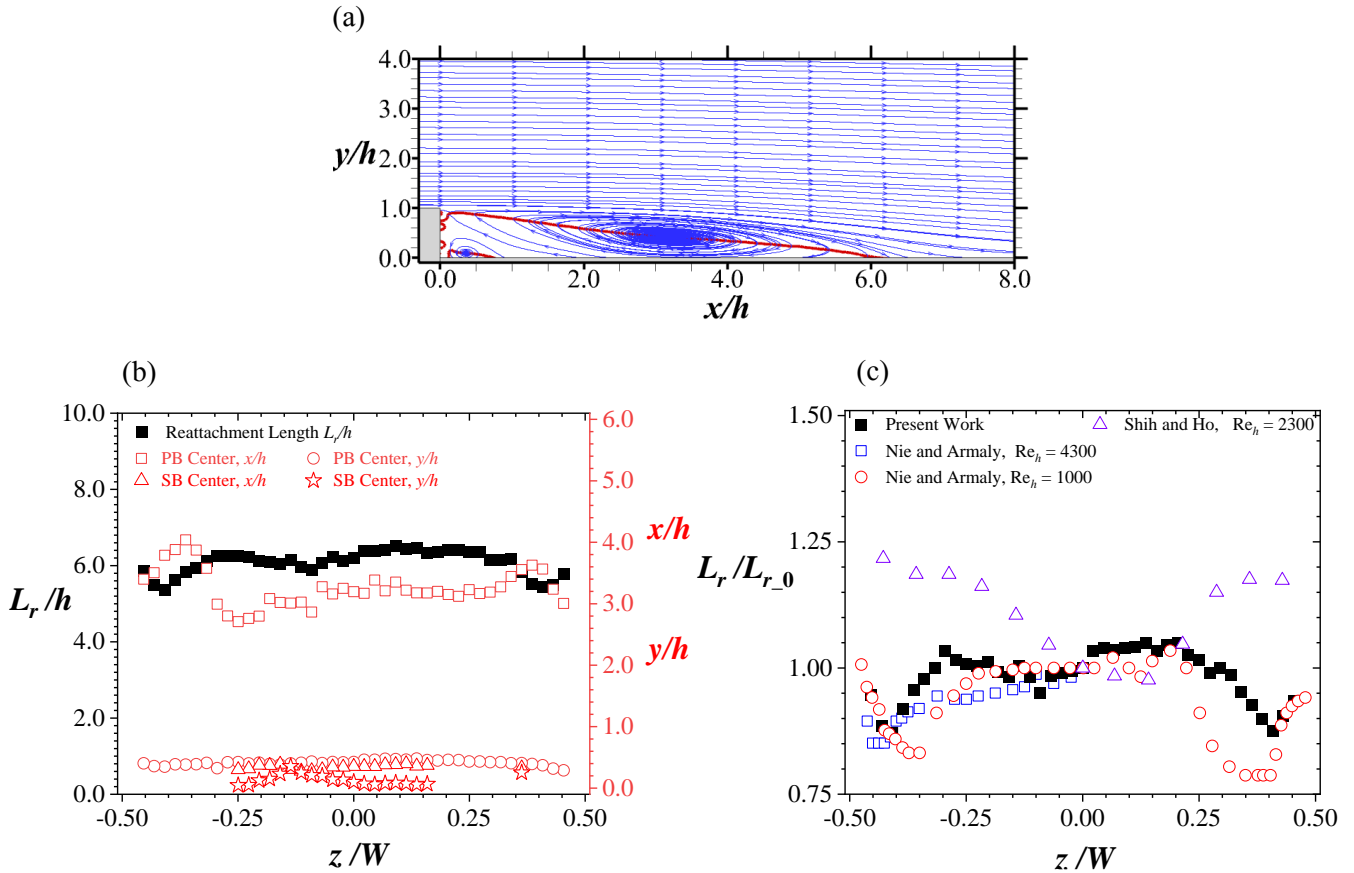


Figure 4: (a) Streamlines of mean velocity (in blue) superimposed with isopleths of zero mean streamwise velocity (in red) of the BFS flow at $z/W = 0$. (b) Reattachment length L_r , primary recirculation bubble (PB) and secondary recirculation bubble (SB) central loci variations with the spanwise coordinate direction z . (c) Present spanwise variations compared with results of Nie and Armaly [24] and Shi and Ho [23]. Note that $L_{r,0}$ is the L_r at the midspan.

To further demonstrate and probe the asymmetric evolution of flow dynamics across the span, planar contour plots of mean and turbulent flow quantities are presented. As shown in Figure 5, the recirculation flow region (i.e. $0 < x/h < 6$) generally decreases in velocity in a direction toward the

sidewalls. However, compared with the positive spanwise direction, the changes in the negative spanwise direction are much more permeating, dramatic, and disruptive, resulting in significantly lower velocities. Thus, as one moves away from the midspan to $z/W = -0.34$ (shown in Figure 5c, d) for instance, the mean velocity contours are less stratified at $y/h > 1$, compared to what prevails in the other direction (i.e. $z/W = 0.34$ shown in Figure 5g, h). Even at a location closer to the sidewalls, the contrast remains. Hence, at $z/W = 0.41$ the mean velocity contours are still structured like the BFS flow in the midspan, albeit with lower velocities. However, at $z/W = -0.41$, the flow communication between the low-flow region behind the step, and the outer layer ($1.5 < y/h < 3$) are so much more effective that the whole flow region records lower velocities compared with $z/W = 0.41$.

The disparities in the mean spanwise vorticity structure close to the sidewalls are also portrayed in Figure 6. In the midspan plane, the narrow-channeled BFS flow is characterized by vorticities due to parcels of fluid rotating or shearing locally. At this plane of measurement, the vorticities radiate from the shoulder of the step, with upper bounds at $y/h < 1.5$. However, at $z/W = -0.41$, the vorticities are dispersed towards the upper wall, while that at $z/W = 0.41$ are tilted towards the lower wall. These observations suggest contrasting vortical structures or activities occurring at either sidewall.

The contours of Reynolds shear stress and planar estimate of the turbulent kinetic energy (i.e. $k \approx 0.75(u^2 + v^2)$) around the recirculation region are also compared in Figure 6. They also generally show differences in turbulence phenomena across various spanwise planes. Specifically, the maximum intensity in Reynolds shear stresses and turbulent kinetic energy are at least twice that at $z/W = -0.41$ compared with $z/W = 0.41$. Additionally, the most intense turbulent motions are directed towards the upper wall at $z/W = -0.41$, in contrast with the lower wall for that at $z/W = 0.41$.

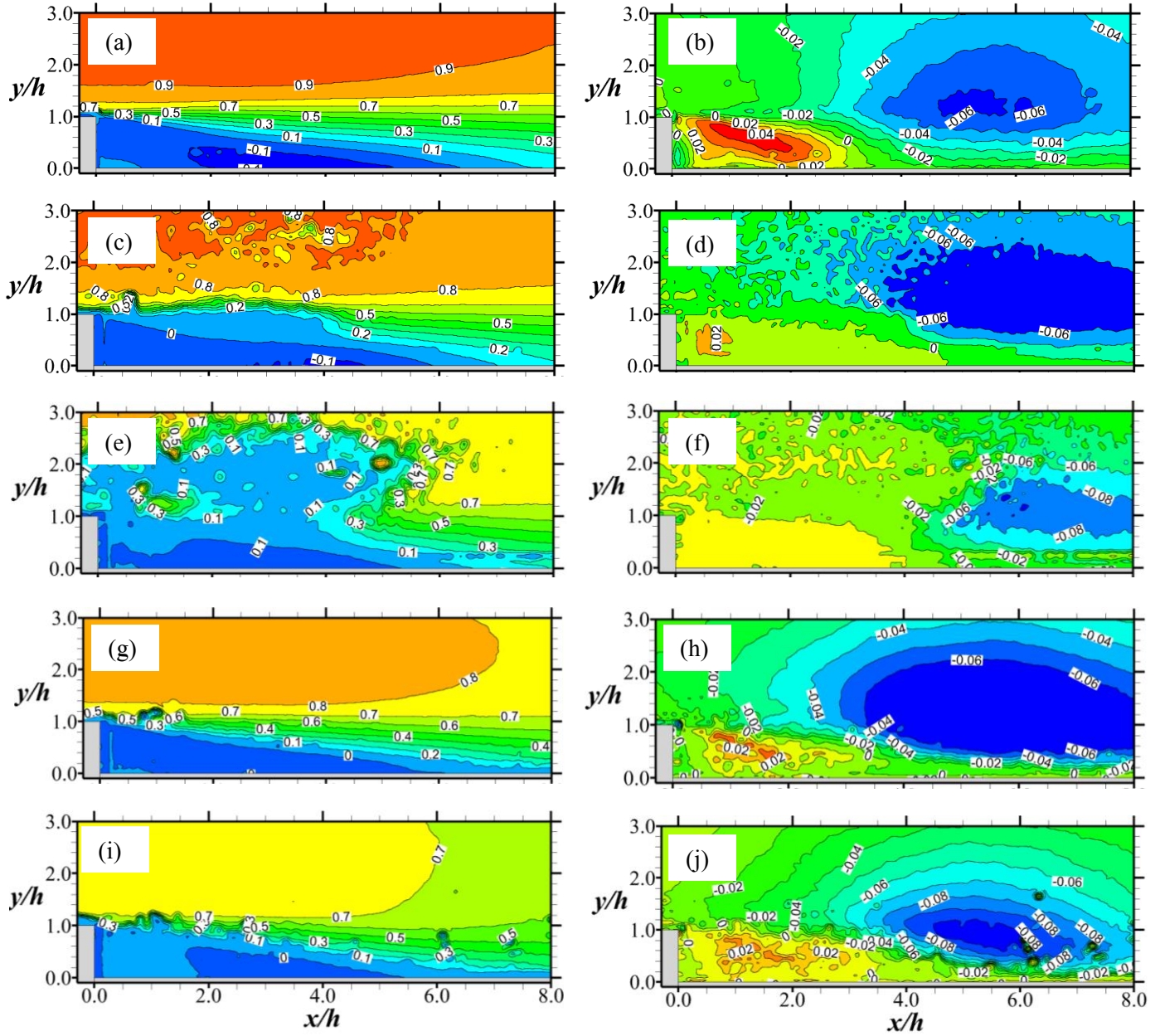


Figure 5: Isocontours of mean streamwise velocity (a, c, e, g, i) and mean wall-normal velocity (b, d, f, h, j) for BFS flow at various spanwise planes. Velocity is normalized by the center-line mean streamwise velocity of the approach flow. Plots in (a, b) are at $z/W = 0$, (c, d) are at $z/W = -0.34$, (e, f) are at $z/W = -0.41$, (g, h) are at $z/W = 0.34$, (i, j) are at $z/W = 0.41$.

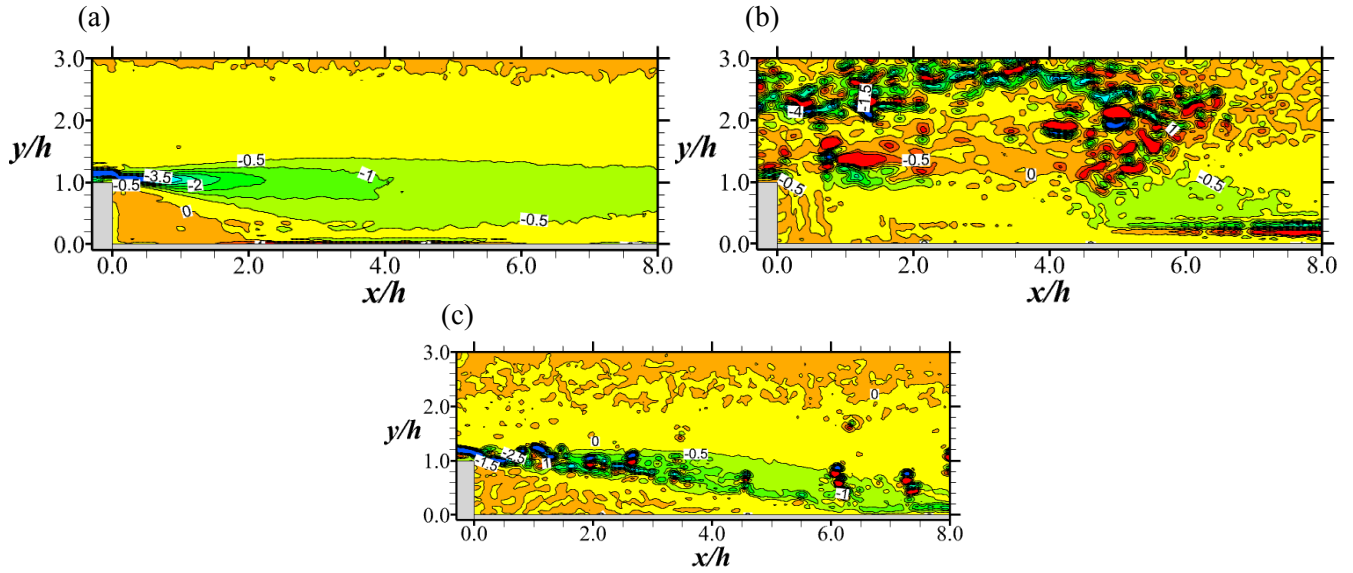


Figure 6: Isocontours of normalized mean spanwise vorticity for plain narrow-channeled BFS flow. Vorticity is normalized by the center-line mean streamwise velocity of the approach flow and the step height. Plot (a) is at $z/W = 0$; (b) is at $z/W = -0.41$; and (c) is at $z/W = 0.41$.

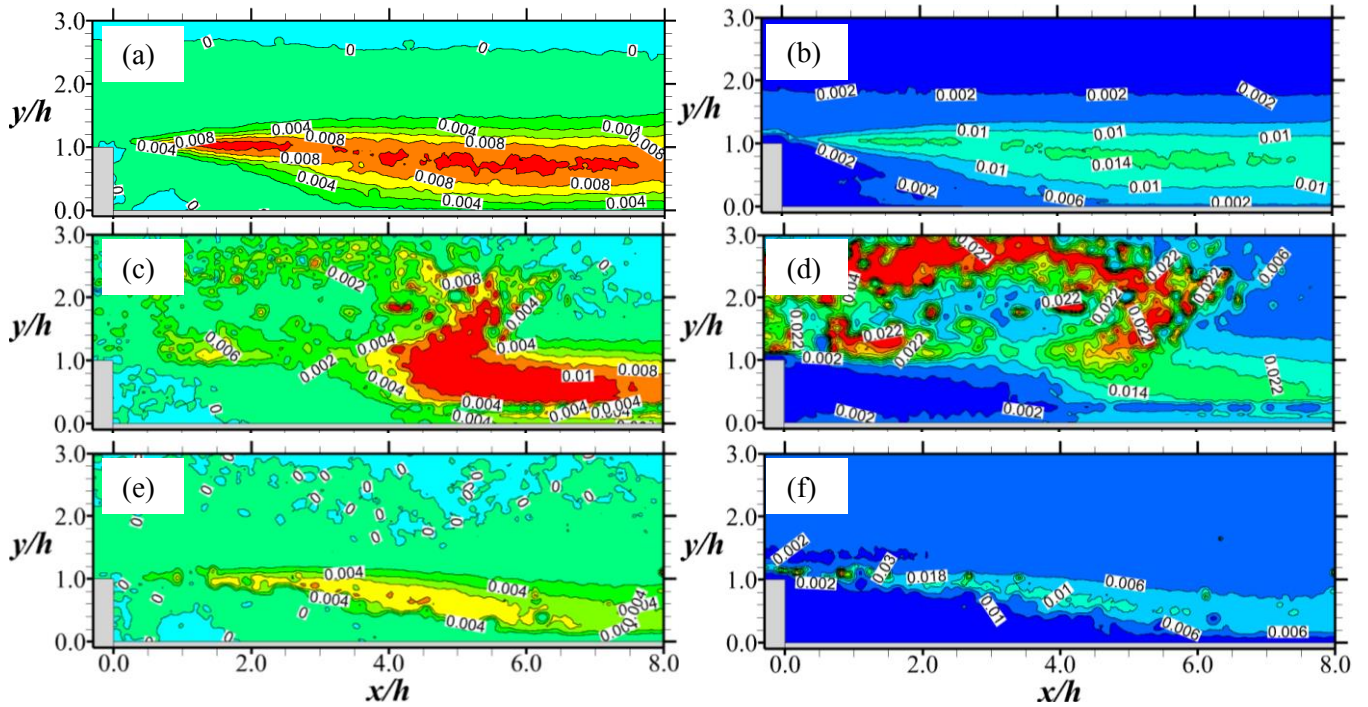


Figure 7: Isocontours of Reynolds shear stress (a, c, e) and turbulent kinetic energy (b, d, f) for plain narrow-channeled BFS flow. Quantities are normalized by the center-line mean streamwise velocity of the approach flow. Plot (a, b) is at $z/W = 0$; (c, d) is at $z/W = -0.41$; and (e, f) is at $z/W = 0.41$.

3.2 Eliminating the Recirculation Region Using a Pin-Fin Insert

Test results from the P-1 model show that by placing the pin-fin rods just behind the step, an elimination of the recirculation zone is achieved. In so doing, the dynamics of the extensive flow-reversal zones associated with BFS flows are radically altered. To demonstrate this, mean velocity contour plots are shown in Figure 8. To understand the data, it is worth noting that the presence of the insert rods channels flow movement just above the lower wall region of the expanded channel into the inter-rod channels of the inserts. This ultimately leads to more streamwise flow uniformity, and consequently, a reduced maximum velocity, indicated by the cut-back in the extent of the maximum isopleth (i.e. 0.9, when compared in Figures 8a and 5a). It is also important to note from Figure 8(b), that no recirculation zones remain in the wake of the insert. All of these changes are reflected in significant increments in wall-normal velocities (compare Figure 8c, d, 5b).

Perhaps, the most obvious changes in the mean flow due to the presence of a pin-fin insert (P-1 model) are evident in the spanwise vorticity isocontours of Figure 8(e, f). Compared with the plain BFS flow (Figure 6a), the maximum vorticity is increased significantly. Furthermore, instead of the peak vorticity localized just downstream of the step shoulder, it is extended over the entire length of the insert. The location and extent of the vorticity is expected, giving that the insert is a model of a porous medium for which vortical activities due to Kelvin-Helmholtz instabilities are rampant [36], [40]. It is also noteworthy that the intensity of the vorticities also declines downstream of the insert. However, the most intense vorticities in the wake of the insert are located at $y/h < 1$, and are higher than those observed in the recovery region of a plain BFS flow.

The salient turbulent statistical attributes of the P-1 model flow are shown in Figure 8. They are limited to contours of Reynolds shear stress (Figure 8 g, h) and planar estimates of the turbulent kinetic energy (Figure 8 i, j). For the Reynolds shear stresses, there are some measured negative Reynolds shear stresses at the upstream locations of the pin-fin rods. This phenomenon has been pointed out in prior studies as characteristic of inward and outward interactions due to fluid motion associated with compact porous media [36], [40]. Additionally, compared with the plain BFS flows, the shear stresses are more subdued downstream of the insert. The turbulent kinetic energy also peaks by as much as three times that attained in the plain BFS flows. The peak values occur also above the rods, as observed in a compact porous medium turbulent flow without a BFS [36].

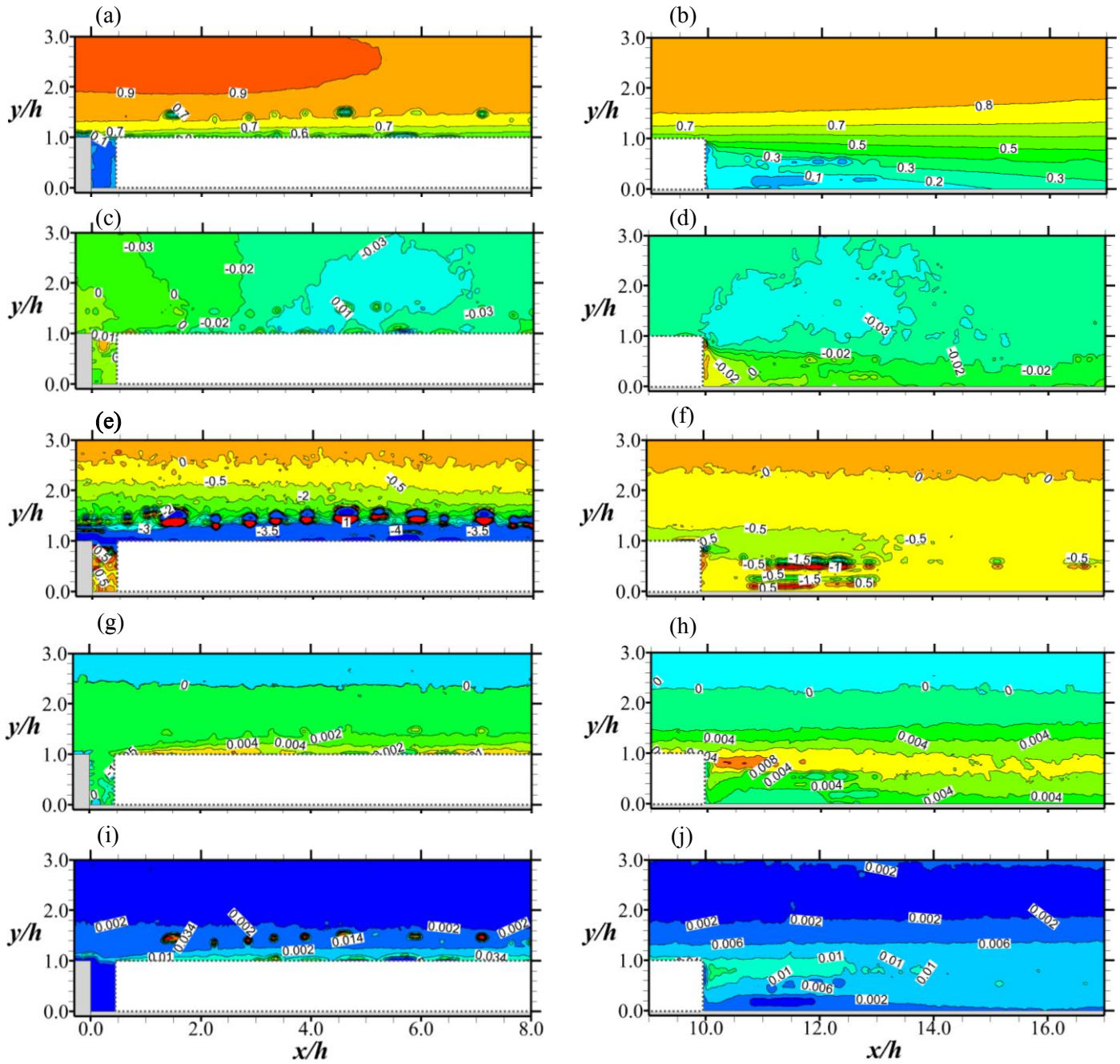


Figure 8: Isocontours of normalized mean streamwise velocity (a, b), mean wall-normal velocity (c, d), mean spanwise vorticity (e, f), Reynolds shear stress (g, h) and turbulent kinetic energy (i, j) for flow in model P-1. All data are obtained in the midspan plane. Quantities are normalized by the center-line mean streamwise velocity of the approach flow and step height, where appropriate. Plots (a, c, e, g, i) are at $-0.3 \leq x/h \leq 8$, and plots (b, d, f, h, j) are at $9 \leq x/h \leq 17$. Note that the white boxes within the plots represent locations of pin-fin inserts.

3.3 Controlling the Recirculation Region Using a Pin-Fin Array Insert

Results of tests conducted using P-3 to P-15 models show that by placing a pin-fin insert at a sufficiently distant location behind the step, the recirculation zone downstream of the BFS flow can be preserved or modified. Thus, the insert affects the resolution of adverse pressure gradient behind the step, serving as a recirculation zone control device by changing its location behind the BFS. This is conclusive from the streamlines plotted in Figure 9. To show this more clearly, the extents of the recirculation region are examined using the reattachment length parameter L_r . In a separate set of evaluation, the streamwise and wall-normal loci of the centers of the primary and secondary bubbles are also determined. The two parameters are plotted in Figure 10 and summarized in Table 2. For completeness, the data for the plain (NP) and P-1 models are included in Table 2.

Comparing Figure 9 with Figure 10, it is evident that there are two stages of control of the recirculation zone. The first stage is represented in Figure 9 (a, b). It corresponds to modulations obtained by placing inserts at $2.9h < m < 6.2h$ (as in P-3 and P-5 models). At such locations, the mean streamlines are marked by a recirculation zone with no corner secondary bubble. As shown in Figures 9 and 10, for this regime, flow modulation is achieved by ‘cutting through’ the primary bubble, culminating in L_r that can be substantially less than the value obtained without a pin-fin rod insert (i.e. $6.2h$). The second stage of recirculation zone control is achieved when insert rods are placed at $m > 6.2h$ (as in P-7, P-9, P-11, P-13 and P-15 models). At such locations, the streamlines of the recirculation zone of the BFS are characterized by primary and secondary bubbles, and L_r can be varied between $6.2h$ and $6.7h$. Thus, at that stage, the insert can act to prevent the attainment of a more favorable pressure gradient. This leads to a separated region that is at least as extended as a plain BFS. This implies that inserts can be leveraged for its extended fin heat transfer benefits without affecting the separated region. However, the limiting effects of such an arrangement will be an added cost in pumping requirement due to pressure drop increment incurred by the insert.

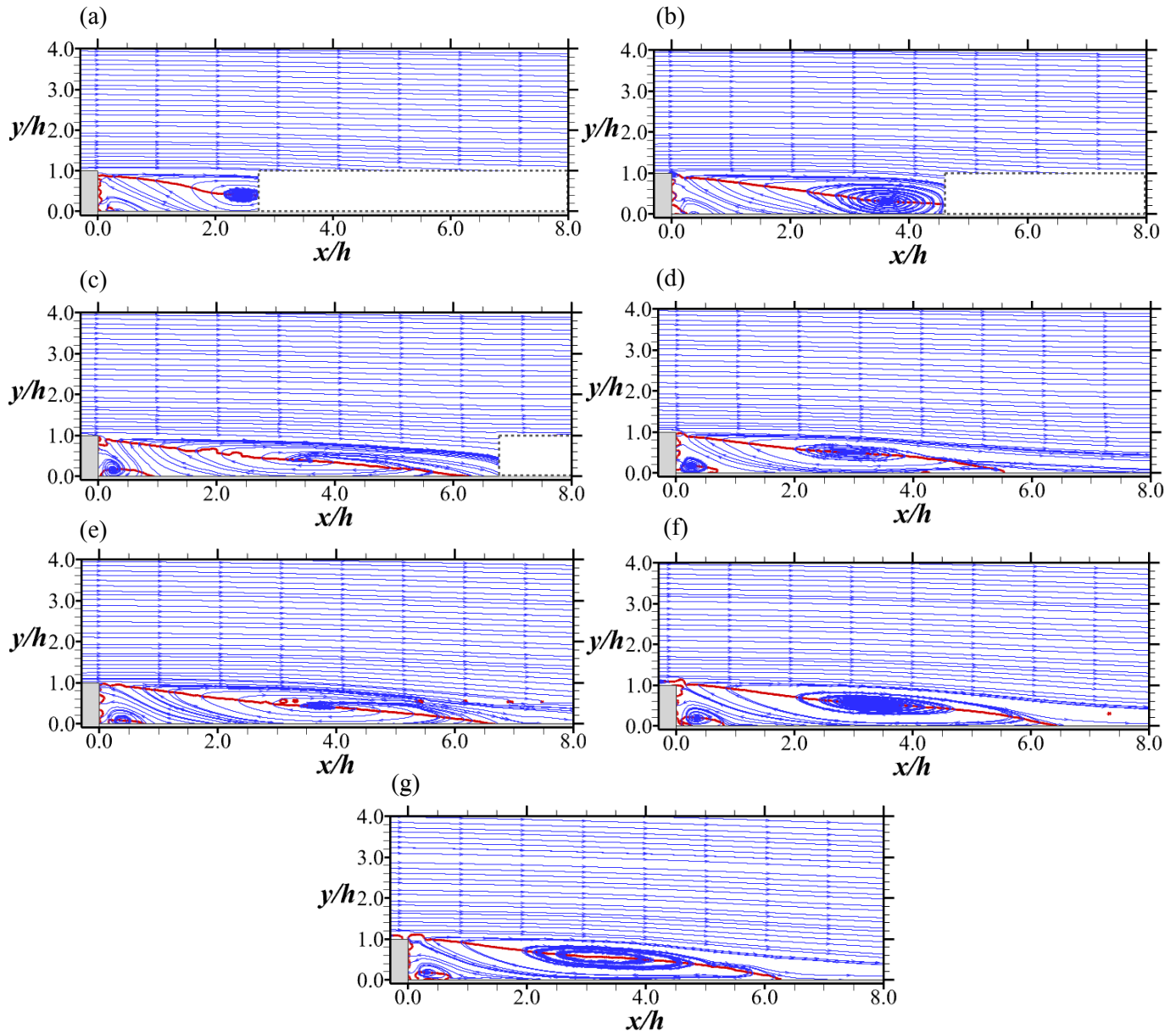


Figure 9: Streamlines of mean velocity (in blue) superimposed with isopleths of zero mean streamwise velocity (in red). Note that (a - g) are respectively plots extracted from measurements for P-3, P-5, P-7, P-9, P-11, P-13 and P-15 models respectively. The white boxes within the plots in (a, b, c) represent locations of pin-fin inserts.

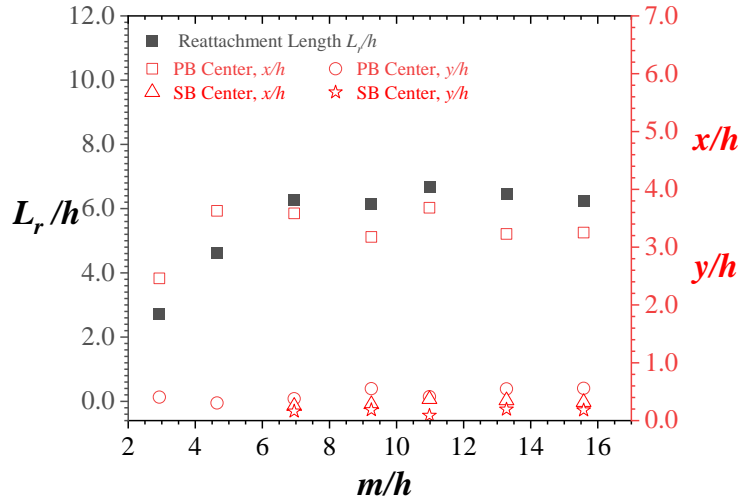


Figure 10: Mean reattachment length L_r , primary recirculation bubble (PB) and secondary recirculation bubble (SB) central loci variations with the streamwise location of the insert m .

TABLE 2: Summary of reattachment length, central loci, and shear layer parameters of the recirculation zone.

Geometric test model	Location of center of most upstream rods from step, m/h	Mean Reattachment length L_r	Primary bubble central locus, x/h	Primary bubble central locus, y/h	Secondary bubble central locus, x/h	Secondary bubble central locus, y/h	Maximum streamwise velocity difference across shear layer ($\Delta U/U_{max}$)	Initial growth rate of vorticity thickness ($d\delta_w/dx$)
NP	-	6.2	3.20	0.42	0.35	0.10	1.21	0.20
P-1	0.63	0.0	-	-	-	-	1.20	0.07
P-3	2.93	2.7	2.46	0.41	-	-	1.18	0.14
P-5	4.65	4.6	3.63	0.31	-	-	1.16	0.16
P-7	6.95	6.3	3.58	0.38	0.25	0.16	1.19	0.16
P-9	9.25	6.2	3.18	0.55	0.28	0.18	1.19	0.24
P-11	10.98	6.7	3.68	0.41	0.37	0.09	1.20	0.21
P-13	13.28	6.5	3.23	0.55	0.35	0.19	1.21	0.21
P-15	15.58	6.2	3.25	0.56	0.32	0.18	1.21	0.20

It is well known that the separated boundary layer of a BFS flow initially responds through instabilities and vortical phenomena confined in a thin layer. Consequently, prior studies have compared the shear layer flow with that of a plane mixing layer [9], [41], [42]. To explore this analogy, parameters used in mixing layer evaluations are employed in more detail analysis of the flow control phenomenon observed in the foregoing. The parameters used are the maximum mean streamwise velocity difference across the shear (ΔU), the maximum mean streamwise velocity gradient across the shear $(\partial U/\partial y)_{max}$, vorticity thickness $\delta_w (= \Delta U / (\partial U/\partial y)_{max})$, and the rate of vorticity thickness $(d\delta_w/dx)$. The results are presented in Table II and Figure 11. For the latter, the local maximum entry streamwise velocity U_{max} , and the mean length of the recirculation zone L_r are the normalizing length and velocity scales, respectively.

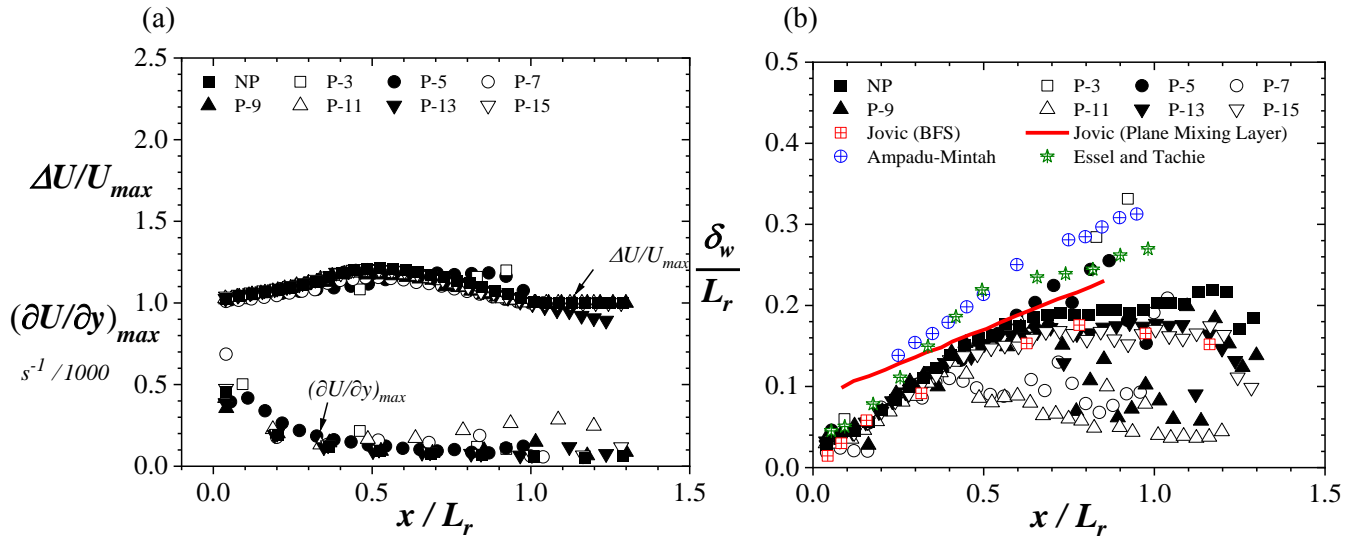


Figure 11: (a) Variation of normalized maximum velocity difference, maximum slope of mean streamwise velocity; and (b) Variation of normalized vorticity length along the streamwise direction compared with published results of Jovic [41], Ampadu-Mintah [42], and Essel and Tachie [9].

Figure 11 highlights several important attributes of the controlled BFS shear layer under study. Firstly, the figure shows that the velocity difference ΔU generally increases to a peak value of $\sim (1.19 \pm 0.3) U_{max}$, and then declines to U_{max} downstream of the reattachment point. The peak

values reported here are lower than that measured in open channel flows over mounted blocks [43]. However, they are comparable with the values stated in other BFS flows in much wider channels [9], [41], [42]. It is also noteworthy from the plots that the velocity gradient $(\partial U/\partial y)_{max}$ follow a similar pattern of post-separation declension as described in other BFS flows [9], [41], [42]. With such conventional trends in velocity difference and gradient, it is therefore not surprising that the distributions of vorticity thickness δ_w in Figure 11 portray shear layers which, like other BFS flows [9], [41], [42], initially grow linearly along the stream, and then break down. The intriguing signal from Table II, however, is that by inserting the pin-fin, the linearities of the vorticity thicknesses can be controlled. Using the growth rate of a plane mixing layer (which has a $d\delta_w/dx$ of 0.16), the control can be classified into two regimes. For the regime where the inserts are located at $m < 6.2h$. (as in P-3 and P-5 models), the shear layer growth rates are lower than that of a plane mixing layer. On the other hand, when the inserts are placed at $m > 6.2h$ (as in P-7, P-9, P-11, P-13 and P-15 models), the shear layer growth rates are at least equal to that of a plane mixing layer. These observations reinforce the idea that the stages of flow control achieved through the use of inserts are not only marked by changes in the recirculation zone size, but by significant variations in shear layer growth rate.

To reveal the distinctive attributes of turbulence, sample one-dimensional plots of Reynolds shear stresses ($-uv$), planar estimates of the turbulent kinetic energy (k) and evaluations of the turbulence production are shown in Figures 12 and 13. As the current measurements are planar, the production term of the turbulent kinetic energy transport equation is assessed as

$$P_k = -u^2 \frac{\partial U}{\partial x} - v^2 \frac{\partial V}{\partial y} - uv \frac{\partial U}{\partial y} - uv \frac{\partial V}{\partial x} \quad (1)$$

To simplify the analysis, only NP, P-3 and P-11 cases at selected locations within the recirculation zone are compared in the figures to demonstrate differences observed for flows associated with a plain BFS, a reduced recirculation zone, and an increased recirculation zone respectively.

It is clear from Figure 12 that $-uv$ and k follow similar trends. The values of turbulent kinetic energy are nonetheless higher than the Reynolds shear stress, showing that the cumulative effects of the Reynolds normal stresses are stronger than the Reynolds shear stresses. As the streamwise Reynolds normal stress (not shown) is the most dominant component of k , it may be inferred that

the main thrust of turbulence is directed along the stream. Overall, the profiles of $-uv$ and k suggest that the Townsend's structure parameter ($-uv/2k$) will have more variation in value (between 0 and 0.20) in the wall-normal direction compared with the streamwise direction. The distribution of k however shows that the placement of a pin-fin insert is capable of generating peak turbulent kinetic energy that is higher than the case without the insert. This particularly prevails when the insert is located further downstream of the step (such as in P-11). Nonetheless, k dampens abruptly thereafter at $y/h < 0.8$ when there is an insert. Specifically, when the inserts are located so close to the step, turbulent energy is insignificant below $y/h < 0.75$. In summary, the $-uv$ and k results indicate that the placement of inserts at locations associated with recirculation reduction tend to decrease turbulent stresses behind the step sharply. On the other hand, the placement of inserts at locations of recirculation extension induces peaks and sharp fluctuations that are not found in plain BFS flows.

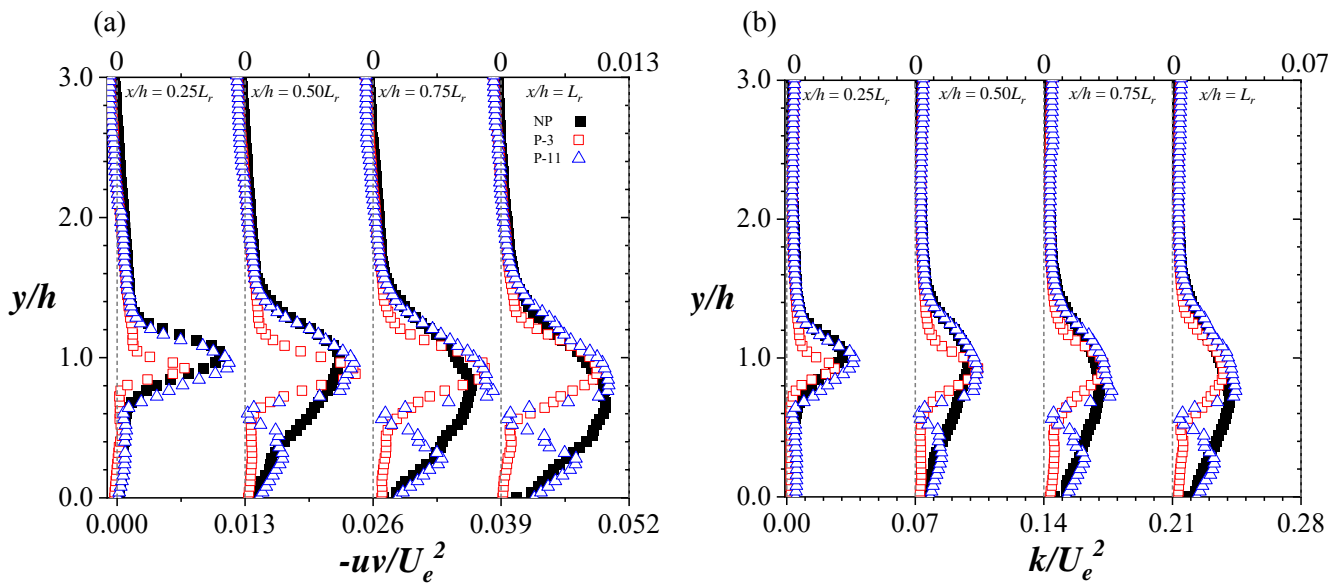


Figure 12: (a) Variation of normalized (a) Reynolds shear stress, and (b) planar estimate of the turbulent kinetic energy. The distributions compare measurements from a plain BFS model (NP), a model with insert located at $m/h = 2.93$ (for P-3) and $m/h = 10.98$ (for P-11) behind the step. The legend in (a) also applies to (b). The turbulent quantities are normalized by the center-line mean streamwise velocity of the approach flow.

The transport equation production term assessments in Figure 13 show that at the region of peak turbulent kinetic energy, the production term is highest for the flows associated with inserts. For both cases, the maximum values increase downstream of the step, as the inserts are approached. A further analysis of the components of the production term shows that the contributions of the shear stresses $P_{k,s}$ (i.e. the sum of the third and fourth terms of equation (1)) are much more dominant compared with the normal stresses $P_{n,s}$ (i.e. the sum of the first and second terms of equation (1)).

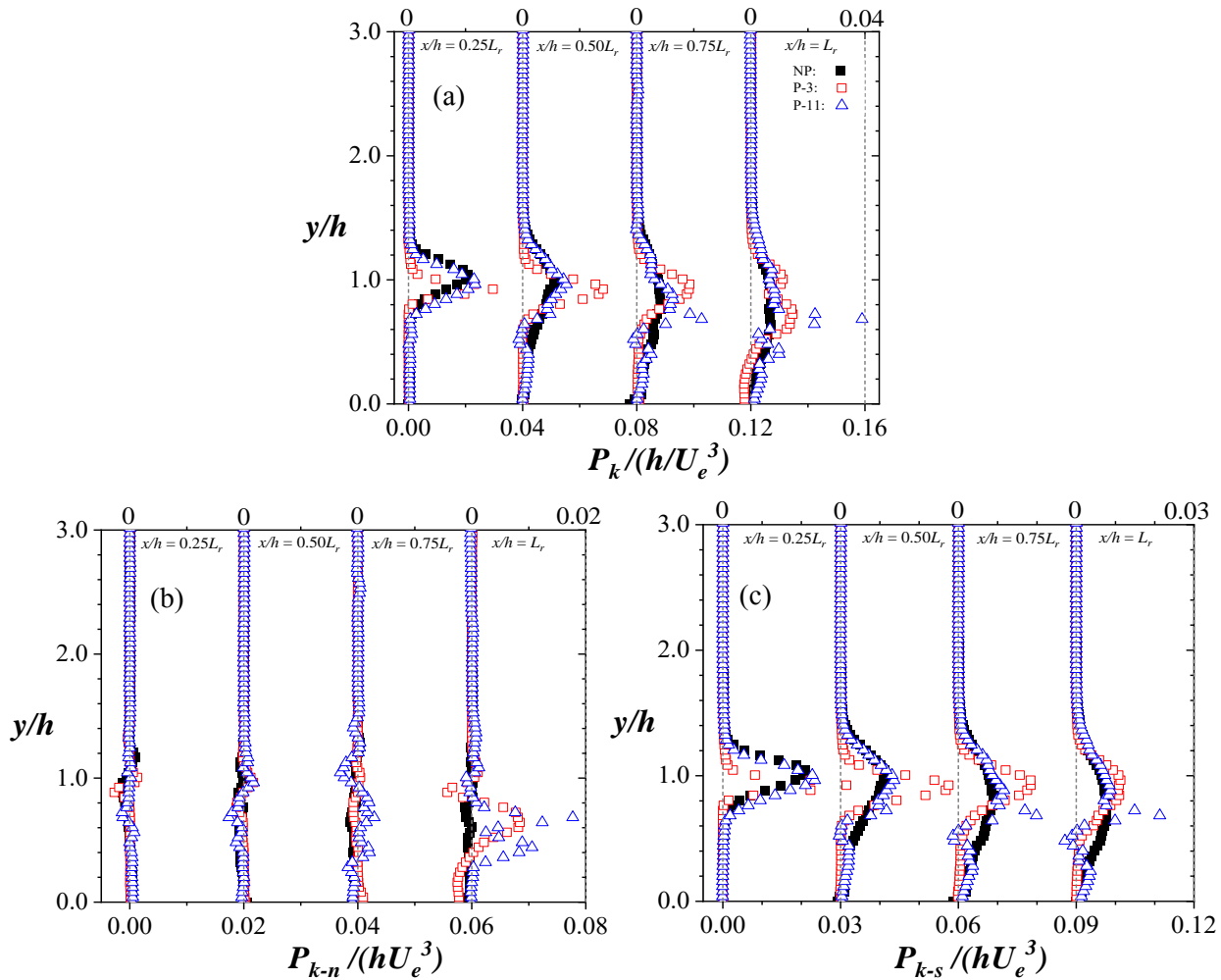


Figure 13: (a) Wall-normal variations of (a) planar production term normalized by the center-line mean velocity of the approach flow and step height (b) normal stress component of the production term, and (c) shear stress component of the production term. The distributions compare measurements from a plain BFS model (NP), a model with insert located at $m/h = 2.93$ (P-3) and $m/h = 10.98$ (P-11) behind the step. The legend in (a) also applies to (b) and (c).

A final observation of interest is that the turbulent production terms change in sign within the recirculation region, and especially in the presence of inserts. This is demonstrated in Figure 14. Such changes imply reversals of the flow of energy between the mean flow and the fluctuating field. While this observation would require a three-dimensional assessment to confirm its validity, it is not a unique observation. The phenomenon of negative turbulent kinetic energy production has been reported to occur in separating and reattaching flow over a blunt body [44]. In the present work, this is found to be principally due to $(-u^2 \partial U/\partial x)$ being less than zero, and resulting in an energy sink. The plots thus indicate that within the separated flow region of a narrow-channeled BFS flow, negative production of turbulence can be intensified depending on the location of the pin-fin rods.

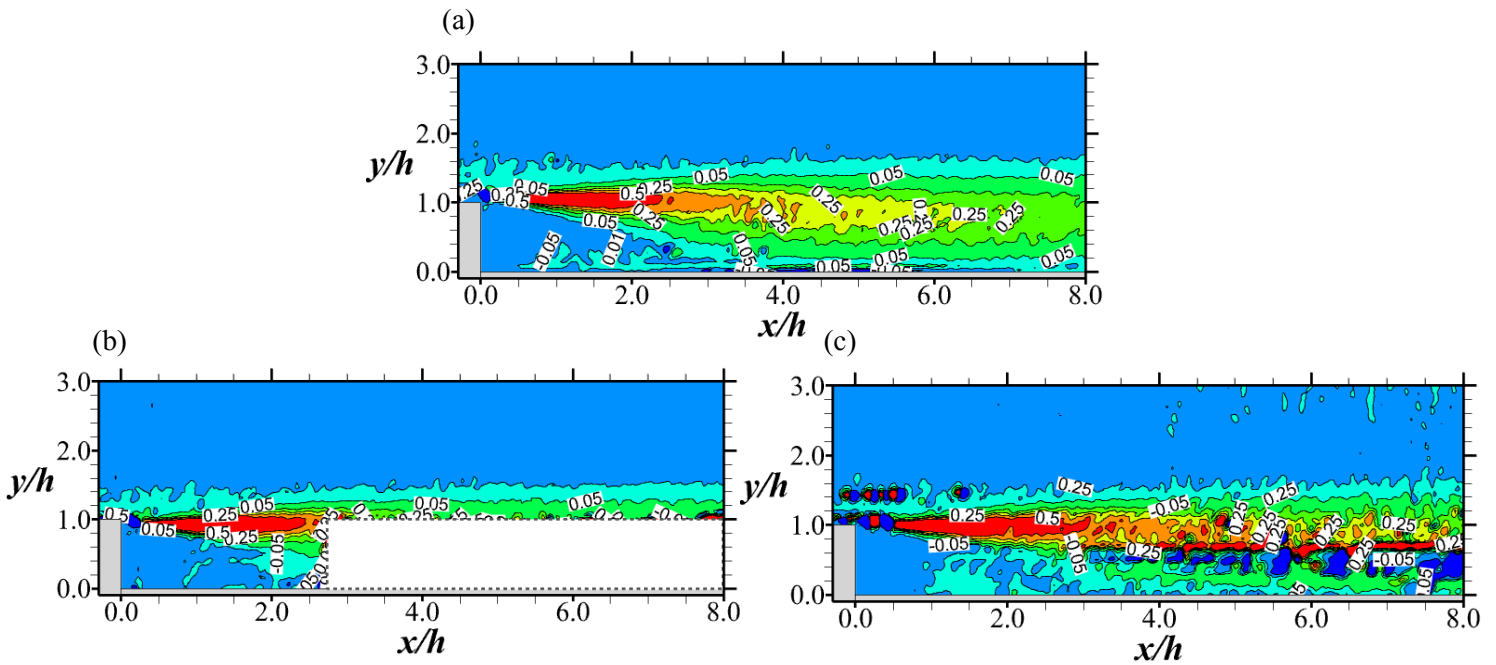


Figure 14: Contours of the planar production term normalized by the center-line mean streamwise velocity of the approach flow and step height for (a) a plain BFS model (NP), (b) a model with insert located at $m/h = 2.98$ (P-3) and (c) model with insert located at $m/h = 10.98$ (P-11) behind the step. Note that the white box within plot (b) represents locations of pin-fin inserts.

4. Conclusion

In this work, a backward-facing step (BFS) flow in a closed narrow channel has been investigated to determine the three-dimensional effects, and the elimination / control of the recirculation region using a porous insert. To accomplish this, several tests of turbulent flows over a BFS closed channel of expansion ratio 1.25, and aspect ratio (AR) 8.0 were carried out. The porous insert was modeled by an array of pin-fin rods of a porosity 85% and of height approximately equal to the step height h . The Reynolds number based on the step height and the center-line mean streamwise velocity, Re_h of ~ 6000 was fixed throughout the tests, while the presence and location of inserts was also varied. Data was obtained using a two-dimensional two-component PIV system.

From this study, a number of conclusions follow. Foremost, that for a BFS flow of $AR = 8$, three-dimensional effects are apparent in the mean and turbulent flow domains, and in variations that are asymmetric about the midspan. Close to the sidewalls, the reattachment length of the recirculation zone can change by 14% (compared to the midspan plane value) and secondary bubbles disappear. However, more vortical activity along with intense turbulent motions are directed towards the upper wall in the negative spanwise plane of the sidewall, compared with the positive spanwise plane.

The data also show that by placing a pin-fin insert directly behind the step, the recirculation zones of BFS flows can be eliminated, leaving no other regions of separation downstream of the insert. However, doing this leads to a radical change in the flow dynamics, resulting in magnified vorticity and turbulence above the insert. On the other hand, by placing the insert at a distance ranging between $2.9h$ and $15.6h$ behind the step, the recirculation zone behind the turbulent BFS flow can be reduced by about 56%, maintained or increased by up to 8%, relative to the case without an insert. For the regime of recirculation reduction, the shear layer growth rate is less than that of a plane mixing layer. For the regime of recirculation maintenance or increment on the other hand, the shear layer growth rate is at least equal to that of a plane mixing layer. The turbulent field indicates that the presence and location of pin-fin inserts may result in magnification of turbulent production and regions of energy sink.

This work is particularly constrained to one AR of BFS flow, and one type of porous insert. Thus, different geometrical parameters, porosities, and structures of porous inserts could lead to different observations. However, the foregoing results have a number of consequential

implications. Firstly, they open up the possibility for a wide range of flow control and heat augmentation utility using porous inserts in narrow-channeled BFS flows. Secondly, they also give further credence to the contribution of pin-fins heat transfer augmentation not merely by the inherent extended surfaces of the rods, but by the enhancement of eddy motion close to the pin-fin rods. Lastly, the results inform us that modeling the flow in the separated region of a narrow-channeled BFS may necessarily have to account for varying Townsend's structure parameter and sign changes in the production terms of the turbulent kinetic energy.

Acknowledgement – The author acknowledges with gratitude the financial support of JKA through the C Graydon and Mary E Rogers Fellowship. The work of the reviewers in providing constructive comments are also appreciated with thanks.

References

- [1] J. K. Eaton and J. P. Johnston, "A review of research on subsonic turbulent flow reattachment," *Aiaa J.*, vol. 19, (9), pp. 1093-1100, 1981.
- [2] V. De Brederode and P. Bradshaw, "Three-dimensional flow in nominally two-dimensional separation bubbles I. Behind a rearward-facing step," *Aeronautical Report*, vol. 19, pp. 72, 1972.
- [3] G. Papadopoulos and M. V. Ötügen, "Separating and reattaching flow structure in a suddenly expanding rectangular duct," *J. Fluids Eng.*, vol. 117, (1), pp.17-23, 1995.
- [4] B. F. Armaly, F. Durst, J. C. F. Pereira and B. Schönung, "Experimental and theoretical investigation of backward-facing step flow," *J. Fluid Mech.*, vol. 127, pp. 473-496, 1983.
- [5] D. M. Driver and H. L. Seegmiller, "Features of a reattaching turbulent shear layer in divergent channel flow," *Aiaa J.*, vol. 23, (2), pp. 163-171, 1985.
- [6] K. Isomoto and S. Honami, "The effect of inlet turbulence intensity on the reattachment process over a backward-facing step," *J. Fluids Eng.*, vol. 111, (1), pp. 87-92, 1989.

- [7] N. Kasagi and A. Matsunaga, "Three-dimensional particle-tracking velocimetry measurement of turbulence statistics and energy budget in a backward-facing step flow," *Int J Heat Fluid Flow*, vol. 16, (6), pp. 477-485, 1995.
- [8] P. M. Nadge and R. N. Govardhan, "High Reynolds number flow over a backward-facing step: structure of the mean separation bubble," *Exp. Fluids*, vol. 55, (1), pp. 1-22, 2014.
- [9] E. E. Essel and M. F. Tachie, "Roughness effects on turbulent flow downstream of a backward facing step," *Flow, Turbulence and Combustion*, vol. 94, (1), pp. 125-153, 2015.
- [10] F. Wang, A. Gao, S. Wu, S. Zhu, J. Dai, and Q. Liao, "Experimental investigation of coherent vortex structures in a backward-facing step flow," *Water*, vol. 11, (12), pp. 2629, 2019.
- [11] J. H. Nie, Y. T. Chen and H. Hsieh, "Effects of a baffle on separated convection flow adjacent to backward-facing step," *International Journal of Thermal Sciences*, vol. 48, (3), pp. 618-625, 2009.
- [12] J. Lai, J. Yue and M. F. Platzer, "Control of backward-facing step flow using a flapping foil," *Exp. Fluids*, vol. 32, (1), pp. 44-54, 2002.
- [13] M. Sano, I. Suzuki and K. Sakuraba, "Control of turbulent channel flow over a backward-facing step by suction," *Journal of Fluid Science and Technology*, vol. 4, (1), pp. 188-199, 2009.
- [14] J. Cheng and Y. Tsay, "Effects of solid and slotted baffles on the convection characteristics of backward-facing step flow in a channel," *Heat and Mass Transfer*, vol. 42, (9), pp. 843-852, 2006.
- [15] W. C. Galuppo and M. J. de Lemos, "Turbulent heat transfer past a sudden expansion with a porous insert using a nonlinear model," *Numerical Heat Transfer, Part A: Applications*, vol. 71, (3), pp. 290-310, 2017.
- [16] Z. Zhao, "Numerical modeling and simulation of heat transfer and fluid flow in a two-dimensional sudden expansion model using porous insert behind that." *Journal of Thermal Analysis & Calorimetry*, vol. 141, pp. 1933-1942, 2020.

- [17] X. B. Chen, P. Yu, S. H. Winoto, and H. T. Low, "Forced convection over a backward-facing step with a porous floor segment," *Numerical Heat Transfer, Part A: Applications*, vol. 53, (11), pp. 1211-1230, 2008.
- [18] J. K. Arthur and O. Schiele, "Numerical analysis of enhanced heat transfer using a pair of similar porous baffles in a backward-facing step flow," *Journal of Fluid Flow, Heat and Mass Transfer (JFFHMT)*, vol. 8, (1), pp. 226-237, 2021.
- [19] B. A. Abu-Hijleh, "Heat transfer from a 2D backward facing step with isotropic porous floor segments," *Int. J. Heat Mass Transfer*, vol. 43, (15), pp. 2727-2737, 2000.
- [20] M. Assato, M. H. Pedras and M. J. De Lemos, "Numerical solution of turbulent channel flow past a backward-facing step with a porous insert using linear and nonlinear k- ϵ models," *J. Porous Media*, vol. 8, (1), pp. 13-30, 2005.
- [21] K. S. Lim, S. O. Park and H. S. Shim, "A low aspect ratio backward-facing step flow," *Exp. Therm. Fluid Sci.*, vol. 3, (5), pp. 508-514, 1990.
- [22] J. G. Berbee and J. L. Ellzey, "The effect of aspect ratio on the flow over a rearward-facing step," *Exp. Fluids*, vol. 7, (7), pp. 447-452, 1989.
- [23] C. Shih and C. Ho, "Three-dimensional recirculation flow in a backward facing step," *J. Fluids Eng.*, vol. 116, (2), pp. 228-232, 1994.
- [24] J. H. Nie and B. F. Armaly, "Reverse flow regions in three-dimensional backward-facing step flow," *Int. J. Heat Mass Transfer*, vol. 47, (22), pp. 4713-4720, 2004.
- [25] M. A. V. Araújo, B. J. Araújo and B. Greenwood, "Acoustic Doppler velocimetry measurements of flow over a backward-facing step," *Journal of Hydraulic Research*, vol. 58, (5), pp. 850-858, 2020.
- [26] J. H. Nie and B. F. Armaly, "Reattachment of three-dimensional flow adjacent to backward-facing step," *J. Heat Transfer*, vol. 125, (3), pp. 422-428, 2003.

- [27] C. Wang, Z. Pinghui, L. Mingzhun, L. Kun, G. Zhihao, L. Jiaming, L. Yuanjie and P. Gang, "DNS of instantaneous behavior in turbulent forced and mixed convection of liquid metal past a backward-facing step," *Flow, Turbulence and Combustion*, vol. 107, (1), pp. 125-147, 2021.
- [28] B. Zajec, M. Matkovič, N. Kosanič, J. Oder, B. Mikuž, J. Kren and I. Tiselj, "Turbulent flow over confined backward-facing step: PIV vs. DNS," *Applied Sciences*, vol. 11, (22), pp. 10582, 2021.
- [29] M. Piirto, A. Karvinen, H. Ahlstedt, P. Saarenrinne and R. Karvinen, "PIV measurements in square backward-facing step," *J. Fluids Eng.*, vol. 129, (8), pp. 984-990, 2007.
- [30] G. L. Juste, P. Fajardo and A. Guijarro, "Assessment of secondary bubble formation on a backward-facing step geometry," *Phys. Fluids*, vol. 28, (7), pp. 074106, 2016.
- [31] H. A. Mohammed, O. A. Alawi and M. A. Wahid, "Mixed convective nanofluid flow in a channel having backward-facing step with a baffle," *Powder Technol*, vol. 275, pp. 329-343, 2015.
- [32] J. K. Arthur, D. W. Ruth and M. F. Tachie, "PIV measurements of flow through a model porous medium with varying boundary conditions," *J. Fluid Mech.*, vol. 629, pp. 343-374, 2009.
- [33] J. K. Arthur, "PIV study of flow through and over porous media at the onset of inertia," *Adv. Water Resour.*, vol. 146, pp. 103793, 2020.
- [34] J. K. Arthur, D. W. Ruth and M. F. Tachie, "Porous medium flow and an overlying parallel flow: PIV interrogation area and overlaps, interfacial location, and depth ratio effects," *Transp. Porous Media*, vol. 97, (1), pp. 5-23, 2013.
- [35] S. Y. Kim and A. V. Kuznetsov, "Optimization of pin-fin heat sinks using anisotropic local thermal nonequilibrium porous model in a jet impinging channel," *Numerical Heat Transfer: Part A: Applications*, vol. 44, (8), pp. 771-787, 2003.
- [36] J. K. Arthur, "Turbulent flow through and over a compact three-dimensional model porous medium: An experimental study," *Fluids*, vol. 6, (10), pp. 337, 2021.

- [37] M. Raffel, C. E. Willert and J. Kompenhans, *Particle Image Velocimetry: A Practical Guide*. 1998 vol. 2.
- [38] B. Wieneke, "PIV uncertainty quantification from correlation statistics," *Measurement Science and Technology*, vol. 26, (7), pp. 074002, 2015.
- [39] R. B. Dean, "Reynolds number dependence of skin friction and other bulk flow variables in two-dimensional rectangular duct flow," *J. Fluids Eng.*, vol. 100, (2), pp. 215-223, 1978.
- [40] J. K. Arthur, "Coherent structures of a turbulent flow bounded by a compact permeable wall," *Fluids*, vol. 7, (5), pp. 158, 2022.
- [41] S. Jovic, "An experimental study of a separated/reattached flow behind a backward-facing step. $Re_h=37,000$," *Nasa Tm-110384*, 1996.
- [42] A. A. Ampadu-Mintah and M. F. Tachie, "Surface roughness effects on separated and reattached turbulent flow in open channel," *Journal of Hydraulic Research*, vol. 53, (3), pp. 302-316, 2015.
- [43] M. Agelinchaab and M. F. Tachie, "PIV study of separated and reattached open channel flow over surface mounted blocks," *Journal of Fluids Engineering*, vol. 130, (6), 2008.
- [44] A. Cimarelli, A. Leonforte, E. De Angelis, A. Crivellini, and D. Angeli, "On negative turbulence production phenomena in the shear layer of separating and reattaching flows," *Physics Letters A*, vol. 383, (10), pp. 1019-1026, 2019.